Temporal constraints on hydrate-controlled methane seepage off Svalbard

C. Berndt[1], T. Feseker[2], T. Treude[1], S. Krastel[1,3], V. Liebetrau[1], H. Niemann[4], V. J. Bertics[1,†], I. Dumke[1], K. Dünnbier[1], B. Ferré[5], C. Graves[6], F. Gross[1], K. Hissmann[1], V. Hühnerbach[6,7], S. Krause[1], K. Lieser[1], J. Schauer[1], and L. Steinle[4]

[1]GEOMAR Helmholtz Centre for Ocean Research Kiel, 24148 Kiel, Germany

[2]MARUM - Center for Marine Environmental Sciences and Faculty of Geosciences, University of Bremen, 28359 Bremen, Germany

[3]now at: Institute of Geosciences, University of Kiel, 24118 Kiel, Germany

[4]Department of Environmental Sciences, University of Basel, 4056 Basel, Switzerland

[5]Department of Geology, University of Tromsø, 9037 Tromsø, Norway

[6]National Oceanography Centre, Southampton, SO14 3ZH, U.K.

[7] now at: GEOMAR Helmholtz Centre for Ocean Research Kiel, 24148 Kiel, Germany

[†]deceased

Methane hydrate is an ice-like substance that is stable at high-pressure and low temperature in continental margin sediments. Since the discovery of a large number of gas flares at the landward termination of the gas hydrate stability zone off Svalbard, there has been concern that warming bottom waters have started to dissociate large amounts of gas hydrate and that the resulting methane release may possibly accelerate global warming. Here, we can corroborate that hydrates play a role in the observed seepage of gas, but we present evidence that seepage off

Svalbard has been ongoing for at least three thousand years and that seasonal fluctuations of 1-2°C in the bottom-water temperature cause periodic gas hydrate formation and dissociation, which focus seepage at the observed sites.

Large quantities of methane, a powerful greenhouse gas, are present in the continental margin West off Svalbard where they are stored as marine gas hydrate (Ref Westbrook, Chabert, Carcione). As hydrate stability is temperature dependent Arctic warming is a potentially major threat to both the environment and the global economy. If even a fraction of the methane contained in Arctic hydrates were released to the atmosphere the effect on climate could be dramatic.

Water column temperature measurements and mooring data suggest a one-degree centigrade bottom water temperature warming for the past thirty years (Ref Westbrook Ferre.[1] [2]) . Numerical modeling of hydrate stability suggests that such warming would result in the dissociation of hydrates in the shallowest sediments[3]. Therefore, the discovery of numerous gas flares, i.e. trains of gas bubbles in the water column, precisely at the water depth where gas hydrate is expected to dissociate[3] was interpreted as the onset of submarine Arctic gas hydrate dissociation in response to global warming which may potentially lead to large-scale escape of methane into the water column and ultimately into the atmosphere. In spite of problems with explaining past rapid warming events by gas hydrate dissociation[4] it should be assessed if anthropogenic warming of the Earth may lead to a large-scale release of methane from gas hydrate and maybe to a positive feedback to global warming.

The margin of Svalbard (Fig. 1) can be considered a model system to study a temperature-related gas hydrate destabilization scenario, as water temperature in the Fram Strait oceanographic gateway will be more affected by changes in global atmospheric temperature than elsewhere in the Arctic and therefore any corresponding changes to a hydrate system should be easier to observe here than elsewhere[5]. The continental margin of Svalbard is characterized by abundant contourite deposits[6] that consist of fine-grained

sediments with high water content which cover most of the margin between water depths of 800 and 3000 m. It is likely that these contourites are underlain by Miocene sediments with 3%wt of total organic carbon as found at ODP Site 909[7]. Proximally, i.e shallower than 700- 800 m water depth, Pleistocene and Pliocene highly heterogeneous, terrigeneous glacial deposits[8, 9]. In the glacial deposits there is only limited evidence for free gas and there is no clear geophysical evidence for gas hydrate such as a Bottom Simulating Reflector. Yet, seismic evidence for gas hydrate occurrence is conclusive for the contourite deposits farther west. In spite of the wide-spread occurrence of geophysical gas hydrate indicators, so far gas hydrate has only been sampled at a vent site in approximately 900 m water depth[10] above a seismic pipe structure that conducts gas through the GHSZ.

Several oceanographic expeditions were able to corroborate the location of the gas flares discovered in 2008. During the MSM21/4 survey in August 2012, we collected a series of PARASOUND 18 kHz parametric echosounder profiles with 40 m spacing around the site of the MASOX observatory site (Fig. 1). A ~40 m footprint of the PARASOUND system at 390 m water depth allowed us to obtain a complete coverage of the flare locations within the area of this survey, which means these data are no longer biased by selection of ship tracks as previous surveys. Our results show that the gas flares align between 380 and 400 m water depth corresponding to the upper limit of the gas hydrate stability zone (GHSZ) considering present day bottom water temperature of around 3°C[11]. Geological structures that may focus gas from deeper parts of the plumbing system are absent (Ref Sudipta). Thus, we interpret this match of gas flare origination depth and the calculated landward termination of the gas hydrate stability zone in the sediments as strong circumstantial evidence for a link between gas hydrate dynamics and gas seepage. At the gas flares, significant amounts of methane are liberated into the water column, leading to bottom water CH_4 concentrations of up to 825 nM and a net flux of methane to the atmosphere (Supl. 3).

One objective of this study was to deduce a minimum age for the onset of marine methane release from the sea floor. For detailed sampling of the gas seeps, we carried out ten dives

78 with the manned submersible JAGO. Our observations substantiate the presence of more
79 than 5 m wide and typically more than 20 to 40 cm-thick outcropping carbonate crusts at
80 the Polarstern (246 m) and the HyBIS (385 m) (Fig. 2) sites; small carbonate nodules at the
81 MASOX site (395 m) were found in gravity cores. We analyzed carbonates from the HyBIS
82 and the MASOX site. The mineralogical composition of the carbonates was heterogeneous
83 and admixed with high amounts of detrital silicates. They were characterized by low $\delta^{13}C$
84 isotope values between -27.1 and -41.4 ‰ V-PDB (Suppl. 2). Consequently, these
85 carbonates can be regarded as an archive of microbially-induced, methane-related
86 authigenic precipitation processes[12] The most reliable single age data were obtained from
87 aragonite dominated surface samples. U/Th isotope measurements and resulting minimum
88 seepage age for the MASOX site imply that significant methane-related precipitation was
89 already occurring at 3 kys BP (Suppl. 2). For comparison, the derived ages for the HyBIS
90 site are overlapping or older, e.g. sample SV-2: 8.2 ± 0.5 kys BP or sample SV-3: 4.6 ± 0.5
91 kys BP. The youngest isochron-based age of approximately 0.5 kys BP was deduced from
92 carbonates of the MASOX sediments at 40 to 50 cm depth below seafloor. Due to changes in
93 the path of methane bearing fluids, inclusion of impurities, and alteration of sample
94 material it was not possible to decipher potential on/off-stages or chemical variation of the
95 seeping fluids beyond the results presented in this paper. Hence, it is possible that seepage
96 strength and transport of methane from the sediment to the water column and atmosphere
97 varied over time.

98 We propose that carbonate formation in this area continues until today, because surface
99 sediments (0-10 cm depth below sea floor) at gas vents both at the HyBIS and the MASOX
100 sites were characterized by high rates of anaerobic oxidation of methane (AOM; max 11.3
101 μmol CH_4 cm^{-3} d^{-1}), which is the driver for carbonate precipitation at methane seeps[12].
102 AOM correlated with high concentrations of methane (max 14800 nM), sulfide (max 11000
103 nM) and total alkalinity (max 29 mEq l-1) in the sediment. Chemosynthetic communities
104 (sulfur bacteria mats and frenulate tubeworms) were present at both sites (Suppl. Fig S4).

Observations of old carbonate crusts directly imply that seepage must have been ongoing at all three sites for a very long time. Detailed paleoceanographic reconstructions for the Svalbard area[5] show a pronounced warming since the end of the 19th century. However, even this 100 year-time span seems too short to explain the observed thicknesses. The ages of the recovered carbonate crusts, which are all significantly older than 100 years support this conclusion. Thus, it is unlikely that an anthropogenic decadal-scale bottom water temperature rise is the primary reason for the origin of the observed gas flares, although it may contribute to keeping gas pathways open longer and further.

During the cruise, we recovered the MASOX observatory, which had been deployed twice for a total of 22 months within a cluster of flares between 390 and 400 m water depth. The observatory contained a bottom water temperature sensor sampling every 15 minutes during both deployments. The recorded time series reveals fluctuations of bottom water temperature between 0.6 and 4.9 °C with lowest temperatures between April and June and highest temperatures between November and March (Fig. 3). In both years, the temperature difference between spring and fall/winter was around 1.5 degrees centigrade, but during the second year, the average bottom water temperature was generally about 0.5 degrees higher than that recorded during the first deployment. The time series implies that there is a strong seasonal change of sea floor temperature.

In order to obtain better constraints on the heat exchange between the sediment and the bottom water, we conducted in-situ sediment temperature and thermal conductivity measurements using a 6 m-long heat flow probe along a transect down the slope. Between 500 and 360 m water depth, our measurements revealed a landward increase in thermal conductivity from 1.5 to 2.6 $Wm^{-1}K^{-1}$ with a maximum around the position of the MASOX observatory. High sediment thermal conductivity, large temporal variability in bottom water temperature, and possibly formation and dissociation of gas hydrates resulted in very irregular sediment temperature profiles, which made it difficult to determine the heat flow along the transect line from our data. Based on our measurements at 500 m water depth, we estimate the regional heat flow to be around 0.05 Wm^{-2}. Given the

comprehensive evidence for seepage this value is likely modulated by convective heat transport.

Based on the recorded bottom water temperature time series and the acquired thermal conductivity data, we developed a two-dimensional model of the evolution of the GHSZ along the transect line. As illustrated in Fig. 3, the seasonal changes in bottom water temperature are accompanied by large lateral shifts of the GHSZ at least within the top 5 meters of surface sediments. During the cycle of a year in which bottom water temperature varies as observed in 2011/12, the volume of the GHSZ varied between a maximum value in summer and a minimum value in winter. During the time period covered by our measurements, the GHSZ was at its maximum in June 2011, when it extended to 360 m water depth. Increasing bottom water temperatures from June until December were accompanied by a retreat of the GHSZ at the seafloor to more than 410 m water depth. In the sub-surface, the GHSZ retreated further until it reached its minimum in March 2012.

The modeling shows that persistent supply of dissolved methane from below the GHSZ in this section of the slope would lead to the formation of hydrate from winter until summer. The newly formed hydrate would dissociate again during the second half of the year and thus augment methane emissions from the seabed both by opening pathways to gas ascending from underneath and by releasing gas from the hydrate phase. The total volume of sediment that was affected by seasonal shifts of the GHSZ amounted to between 3000 and 5000 m^3 per meter of the margin. Assuming a gas hydrate concentration of 5 percent of the pore space and a porosity of 50 percent, the seasonal GHSZ has the potential to periodically store and release between 9 and 15 tons of CH_4 per meter of the margin. However, these amounts represent merely the upper limits of the seasonal buffering capacity, as the latent heat of hydrate kinetics was not included in the simulation. Depending on the concentration and distribution of gas hydrates in the sediment, alternating formation and dissociation would dampen the oscillation of the GHSZ and thus reduce its volume.

While the modeling shows clearly that seasonal bottom water temperature variations are capable of modulating the observed gas emissions, we find no direct evidence in the heat flow data that would suggest that the slope sediments experienced decadal-scale warming. The combined data demonstrate that hydrate is playing a fundamental role in modulating gas seeps between 380 and 400 m water depth at the upper limit of the gas hydrate stability zone, while ascending gas would be trapped or deviated up along the base of the GHSZ further seaward. Long-term variations in seepage may exist but presently available data are insufficient to document annual, decadal or centennial changes in seepage. Our data suggest that shallow hydrate accumulations are sensitive to bottom water temperature changes and therefore significant anthropogenic warming will impact the shallow parts of the hydrate system. This sensitivity demonstrates the need for quantifying the total amount of gas hydrate in the shallowest part of the gas hydrate stability zone if climate feedback mechanisms are to be assessed beyond simple global models[13, 14].

Acknowledgments

We are grateful to Captain K. Bergmann and the officers and crew of R/V MARIA S. MERIAN for their help at sea. The German Research Foundation DFG, the Swiss National Science Foundation, and the Cluster of Excellence "The Future Ocean" supported the project financially. Further support came from the PERGAMON project (COST) and the Alexander von Humboldt Foundation. Figure 1 was drafted using GMT[15].

Supplementary Materials

www.science.org

Materials and Methods

References

Movie

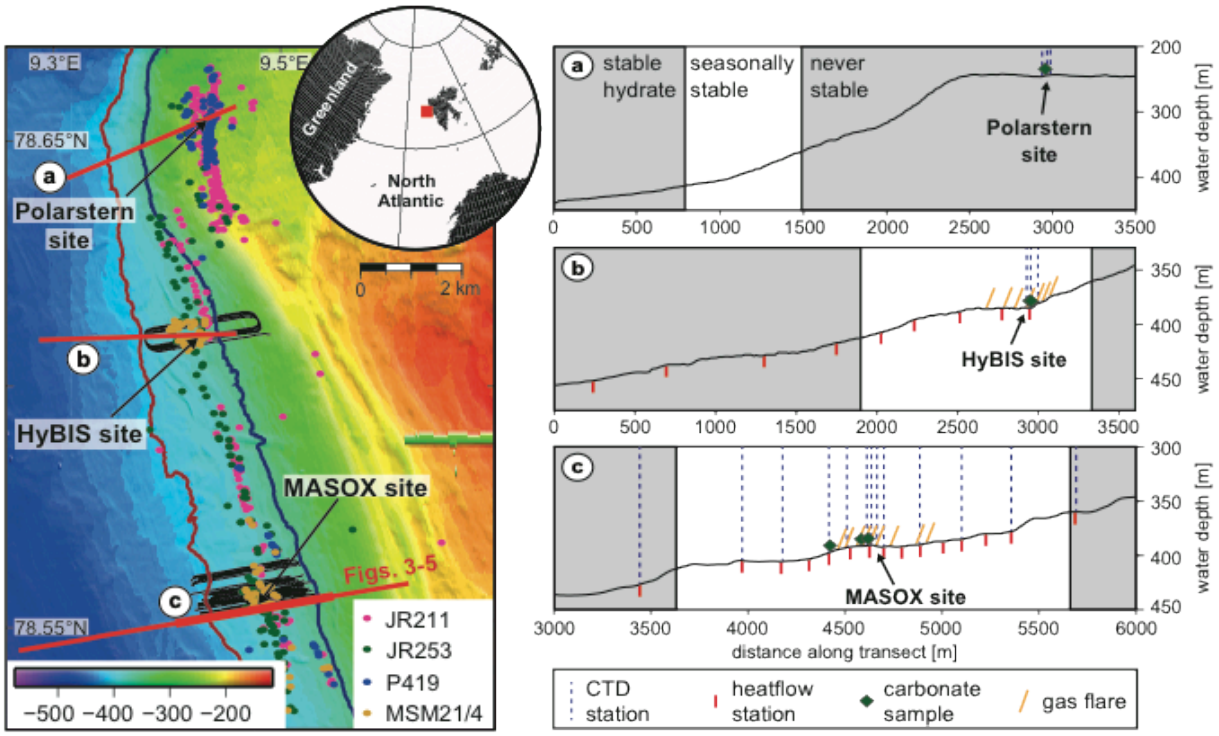

184

185

186 **Fig. 1**. The Svalbard gas hydrate province is located on the western margin of the Svalbard
187 archipelago (inset). At water depths shallower than 398 m numerous gas flares have been
188 observed in the water column (color-coded dots for different surveys) using EK60 echo
189 sounders and high-resolution side scan sonar. The gas flares are located between the
190 contour lines at which gas hydrate is stable in the subsurface at 3 (brown) and 2 (blue)
191 degrees C average bottom water temperature. The black lines show the location of
192 PARASOUND profiles with 40 m separation, i.e. complete coverage, for flare mapping. The
193 white arrows point to the location of submarine dives discussed in the text. The red line
194 shows the location of the modeling transect (bold section shown in Fig. 3). The large cluster
195 of seeps at the northern limit of the gas flare line at a water depth of 240 - 260 m, can be
196 explained by the presence of an elsewhere absent glacial debris flow deposit that is
197 deviating gas laterally within the prograding debris flow deposits and cannot have
198 anything to do with gas hydrate dynamics[6,16].

Fig. 2. Photograph of the massive authigenic carbonate crusts observed at the HyBIS site in 385 m water depth. For scale, the total length of the larger white sessile ascidia (white stalk-like animal on the crest of the uplifted carbonate plate) is approximately 15 cm. Carbonate crusts such as these take at least several hundred years to develop through anaerobic oxidation of methane.

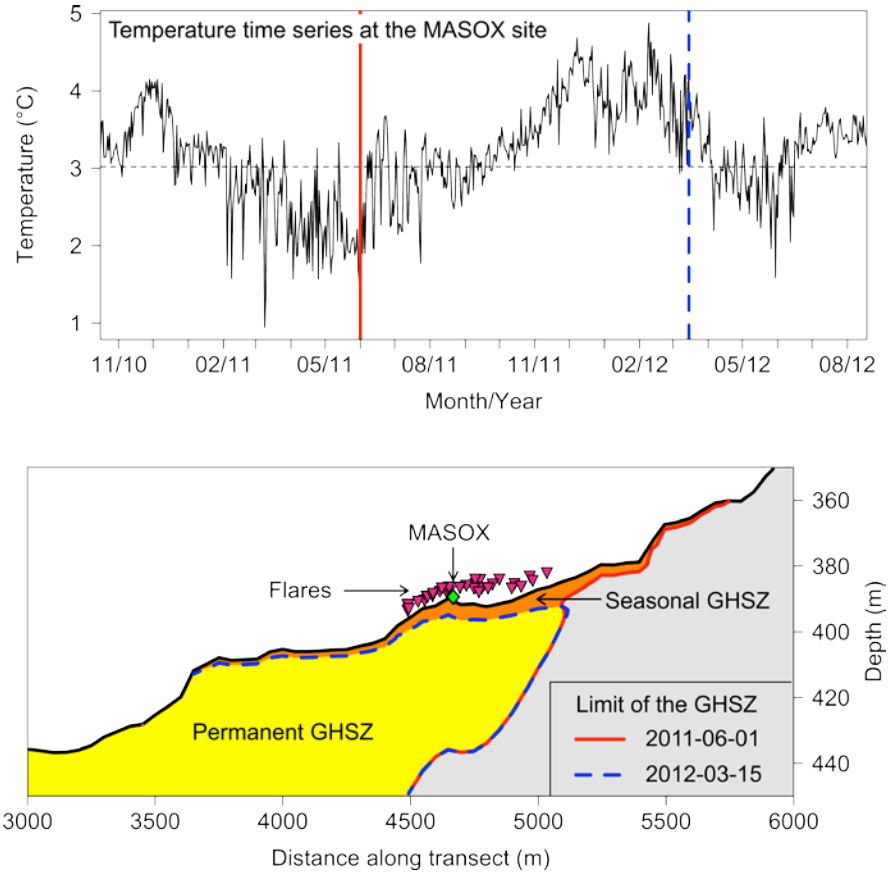

205

206 **Fig. 3.** The top panel shows daily means of bottom water temperature recorded by the
207 MASOX observatory. The times when the extent of the GHSZ was at its maximum and
208 minimum are marked by the solid red and dashed blue lines, respectively. The bottom
209 panel shows the seasonal dynamics of the GHSZ. Driven by changes in bottom water
210 temperature, the GHSZ advances and retreats in the course of the year. The solid red lines
211 and the dashed blue lines indicate the maximum and minimum extent of the GHSZ,
212 respectively. The area in which gas hydrates are stable in the long-term is shaded in yellow.
213 The difference between the maximum and minimum extent of the hydrate stability zone is
214 shaded in orange and corresponds to the seasonal GHSZ, in which gas hydrate dissociation
215 and formation alternate periodically. The triangles filled in magenta represent the
216 projected locations of all flares detected within 1000 m of the transect line. The green
217 diamond shows the position of the MASOX observatory. An animated illustration of the
218 modeling results is provided in the supplements.

References

1. G. K. Westbrook *et al.*, Escape of methane gas from the seabed along the West Spitsbergen continental margin. *Geophys. Res. Lett.* **36**, (2009).
2. B. Ferré, J. Mienert, T. Feseker, Ocean temperature variability for the past 60 years on the Norwegian-Svalbard margin influences gas hydrate stability on human time scales. *Journal of Geophysical Research: Oceans* **117**, n/a-n/a (2012).
3. K. E. Thatcher, G. K. Westbrook, S. Sarkar, T. A. Minshull, Methane release from warming-induced hydrate dissociation in the West Svalbard continental margin: Timing, rates, and geological controls. *Journal of Geophysical Research: Solid Earth* **118**, 22-38 (2013).
4. G. R. Dickens, Down the Rabbit Hole: toward appropriate discussion of methane release from gas hydrate systems during the Paleocene-Eocene thermal maximum and other past hyperthermal events. *Clim. Past* **7**, 831-846 (2011).
5. R. F. Spielhagen *et al.*, Enhanced Modern Heat Transfer to the Arctic by Warm Atlantic Water. *Science* **331**, 450-453 (2012).
6. O. Eiken, K. Hinz, Contourites in the Fram Strait. *Sedimentary Geology* **82**, 15-32 (1993).
7. J. Knies, U. Mann, Depositional environment and source rock potential of Miocene strata from the central Fram Strait: introduction of a new computing tool for simulating organic facies variations. *Marine and Petroleum Geology* **19**, 811-828 (2002).
8. T. O. Vorren, E. Lebesbye, K. Andreassen, K. B. Larsen, Glacigenic sediments on a passive continental margin as exemplified by the Barents Sea. *Marine Geology* **85**, 251-272 (1989).
9. A. Solheim, E. S. Andersen, A. Elverhøi, A. Fiedler, Late Cenozoic depositional history of the western Svalbard continental shelf, controlled by subsidence and climate. *Global and Planetary Change* **12**, 135-148 (1996).
10. R. E. Fisher *et al.*, Arctic methane sources: Isotopic evidence for atmospheric inputs. *Geophysical Research Letters* **38**, L21803 (2011).
11. S. Sarkar *et al.*, Seismic evidence for shallow gas-escape features associated with a retreating gas hydrate zone offshore west Svalbard. *Journal of Geophysical Research* **117**, B09102 (2012).
12. R. Luff, K. Wallmann, G. Aloisi, Numerical modeling of carbonate crust formation at cold vent sites: significance for fluid and methane budgets and chemosynthetic biological communities. *Earth and Planetary Science Letters* **221**, 337-353 (2004).
13. D. Archer, B. A. Buffett, Time-dependent response of the global ocean clathrate reservoir to climatic and anthropogenic forcing. *Geochemistry Geophysics Geosystems* **6**, doi:10.1029/2004GC000854 (2005).
14. A. Biastoch *et al.*, Rising Arctic Ocean temperatures cause gas hydrate destabilization and ocean acidification. *Geophysical Research Letters* **38**, L08602 (2011).

15. P. Wessel, W. H. F. Smith, Free software helps map and display data. *EOS* **72**, 441, 445-446 (1991).
16. P. Tishchenko, C. Hensen, K. Wallmann, C. S. Wong, Calculation of the stability and solubility of methane hydrate in seawater. *Chemical Geology* **219**, 37-52 (2005).
17. P. M. Saunders, Practical conversion of pressure to depth. *Journal of Physical Oceanography* **11**, 573-574 (1981).

Supplementary materials

Supplement 1: Numerical model of the GHSZ

The MASOX observatory was deployed at 396 m water depth from 2010-10-15 until 2011-08-05 and at 389 m water depth from 2011-08-08 until 2012-08-18. The observatory contained a CTD, which acquired bottom water temperature measurements every 15 minutes during both deployments. The two time series were merged into one, the resolution was reduced to daily means, and the three-day gap between the deployments of the observatory was interpolated. We selected the time interval from 2010-10-16 until 2011-10-16 as a generic annual time series because of the very small temperature difference between start and end (Fig. 3) noticing however, that the absolute temperature may be offset from the long-term average. The resulting time series was repeated for the duration of the modeling time and applied as a changing temperature boundary condition at the seafloor in a two-dimensional finite element model of time-dependent heat conduction in COMSOL Multiphysics.

The model domain comprised a 7.5 km-long transect orthogonal to the slope from 502 to 214 m water depth and reached down to 600 m depth below sea floor (Fig. S1). Using a 6 m-long heat flow probe, we conducted in situ thermal conductivity measurements at 26 stations along the transect line. The measurements were evaluated according to Villinger and Davis (1987). The thermal conductivity along this section of the slope varied between 1.5 and 2.6 $Wm^{-1}K^{-1}$ (Fig. S2). Using the mixing model of Woodside and Messmer (1961) and assuming values of thermal conductivity of 0.6 $Wm^{-1}K^{-1}$ for the pore water and 5 Wm^{-}

289 $^{1}K^{-1}$ for the quartz-rich solid phase, the range of thermal conductivity of the bulk sediment
290 may be explained by values of porosity of between 34 and 57 percent.

291 The remaining properties of the sediment in the numerical model were defined according
292 to this porosity model (Table S1). All properties are constant in the vertical direction, but
293 vary in the horizontal direction.

294 Based on our in situ sediment temperature measurements at 500 m water depth, the heat
295 flow across the lower boundary into the model domain was set constant to 0.05 Wm^{-2}. Both
296 sides of the model domain were thermally insulated. The length of the time steps was
297 limited to a maximum of half a day and at the seabed boundary, the cell size of the finite
298 element mesh was limited to one square meter.

299 In order to eliminate artificial long-term changes during the simulation, the initial
300 temperature distribution in the model was chosen to be in equilibrium with the median
301 value of the generic annual bottom water temperature time series (3.01757 °C). The same
302 time series was applied repeatedly for thirty years of modeled time, such that changes
303 between successive years were negligible. During the 31st and 32nd year of the simulation,
304 the bottom water temperature time series obtained from the two deployments of the
305 MASOX observatory was applied as bottom water temperature boundary condition. The
306 limit of the GHSZ was determined for the beginning and the middle of each month,
307 assuming pure methane hydrates, a salinity of 35 PSU, and sulfate-free pore water[*16*],
308 which is consistent with the coring results. Pressure was converted to depth following
309 Saunders[*17*] and taking into account a standard atmospheric pressure of 101325 Pa. The
310 consumption and release of heat during hydrate dissociation and formation, respectively,
311 were not included in the simulation.

312

313

314 **Table S1**: Parameters of the numerical model

	Parameter	Value
p_{Atm}	atmospheric pressure	101325 Pa
q	background heat flow	0.05 W m^{-2}
T_0	initial bottom water temperature	3.01757 °C
k	thermal conductivity of the bulk sediment	1.50 to 2.44 W m^{-1} K^{-1}
k_w	thermal conductivity of water	0.6 W m^{-1} K^{-1}
k_s	thermal conductivity of sediment grains	5 W m^{-1} K^{-1}
$\phi = \log(k/k_s)/\log(k_w/k_s)$	porosity	0.34 to 0.57
c_w	specific heat capacity of water	4184 J $kg^{-1}K^{-1}$
c_s	specific heat capacity of sediment grains	300 J $kg^{-1}K^{-1}$
$c = c_w * \phi + c_s *(1- \phi)$	specific heat capacity of bulk sediment	1614 to 2505 J $kg^{-1}K^{-1}$
ρ_w	density of water	1025 kg m^{-3}
ρ_s	density of sediment grains	2650 kg m^{-3}
$\rho = \rho_w * \phi + \rho_s *(1- \phi)$	density of bulk sediment	1727 to 2100 kg m^{-3}

315

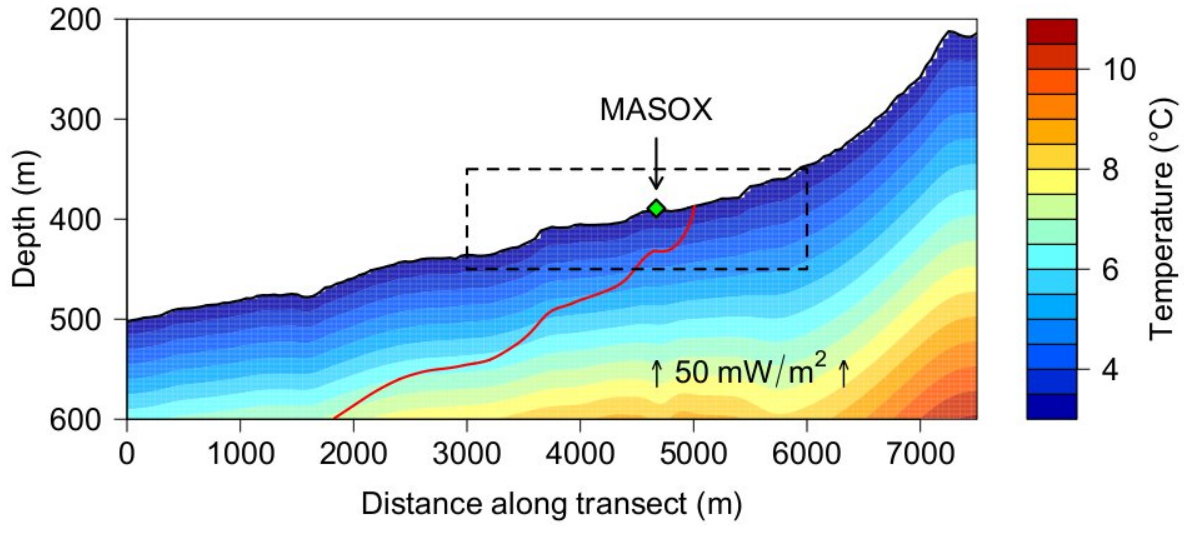

316

Fig. S1: Setup and initial temperature distribution of the numerical model. The lower boundary condition was a constant heat flow of 0.05 Wm^{-2} into the model domain. Both sides of the model domain were thermally insulated. During each time step, the temperature along the entire seabed boundary was constant. At the start of the simulation, the temperature distribution in the sediment was in equilibrium with the median value of the bottom water temperature in a generic year. The solid red line shows the corresponding limit of the GHSZ. The dashed lines mark the section of the model domain that is shown in Fig. 3 and in the animation.

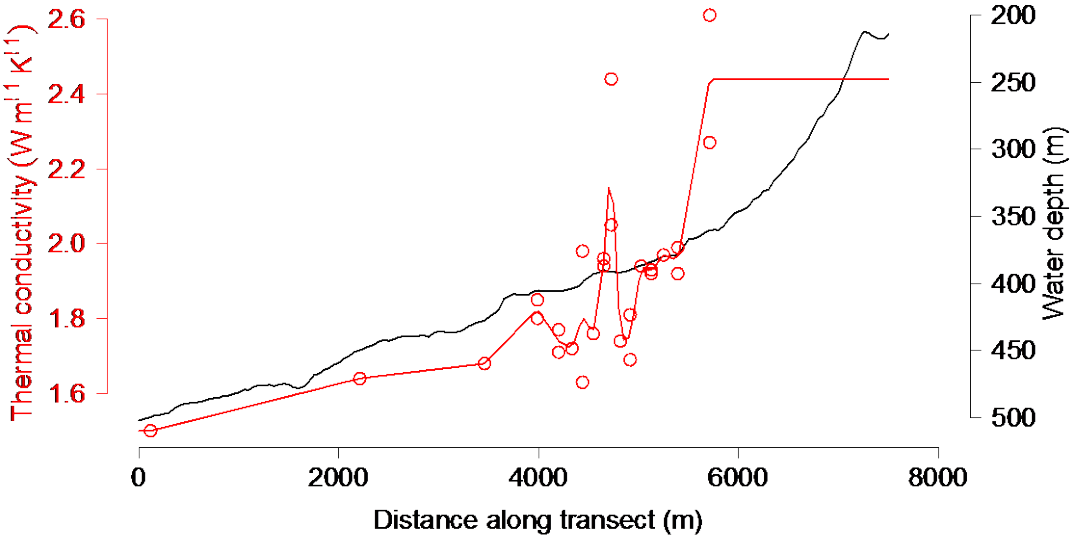

Fig. S2: Thermal conductivity of the sediment and water depth along the transect line. The red circles indicate the results of in situ measurements using the 6 m-long heat flow probe. The red line represents the values used in the numerical model.

See file: cberndt-animation.mpg

Animation: Evolution of the GHSZ in response to bottom water temperature changes. The bottom water temperature and the relative volume of the GHSZ per m of the slope are shown at the top, where the vertical red lines indicate the values corresponding to the time

slice of the simulation illustrated below. The green part of the bottom water temperature data in 2010 marks data that was generated by copying the measurements obtained in 2011. The dashed horizontal line in the bottom water temperature graph shows the median value for a generic year. For each time slice, the area shaded in yellow and bounded by the red lines shows the section of the sediment in which pure methane hydrates are stable. The projected locations of all flares within 1000 m of the transect line are represented by blue open triangles in the last time slice of the simulation.

Supplement 2: U-Th geochronology & light stable isotopes of authigenic carbonates

Material and Methods

Sample material and sub-sampling

During R/V Maria S. Merian cruise MSM 21/4 massive carbonates and carbonate-enriched sediments were sampled by the submersible JAGO and by gravity coring (GC). Here, we present the analysis of surface and gravity corer samples from the MASOX site. They presumably represent the least mature authigenic precipitates from the deepest active methane emanation site sampled during MSM-21/4. As reference two samples from the HyBIS site are also presented.

Samples were dried at 20°C for 12 hrs and gently cleaned from loosely bound sediment remains. Homogeneous subsamples were collected by drilling material from solidified samples by a handheld mm-sized mini-drill and from less consolidated surrounding sediments. From the solidified samples the surface of each sub-sampling spot was scoured away in an area of ~5 x 5 mm. Subsequently, the original sample powder was extracted by drilling small cavities. Prior to aliquot procedures all samples were finely ground in an agate mortar providing homogeneous aliquots of suitable grain size for the combined approach of mineral identification by X-ray diffractometry (XRD), $\delta^{18}O$ and $\delta^{13}C$ analyses by

stable isotope ratio mass spectrometry (SIRMS) as well as for U-Th geochronology by multi collector-inductively coupled plasma-mass spectrometry (MC-ICP-MS).

X-ray diffraction analyses

We analyzed representative aliquots and semi-quantitatively identified minerals using x-ray diffraction (XRD) with a Philips X-ray diffractometer PW 1710 in monochromatic CuKα mode between 2 and 70 2θ (incident angle). Note, especially on small sample aliquots of few 10 mg as required in this study relative quantifications are generally accompanied by large uncertainties. Furthermore, the sensitivity for mineral identification is typically restricted to fractions greater than 5% and significant amounts remained not identified. Resulting spectra were analyzed with the software XPowder (XPowder, Spain).

Light stable isotope analysis ($\delta^{18}O$ and $\delta^{13}C$)

From each homogenized carbonate powder sample (see above), an aliquot of 10 mg was separated for carbon $\delta\ ^{13}C$ and oxygen $\delta^{18}O$ stable isotope analysis. A small part (approximately 1 mg) of this powder was dissolved by water-free phosphoric acid at 73°C in a "Carbo-Kiel" (Thermo Fisher Scientific) online carbonate preparation line and measured for carbon and oxygen stable isotope ratios with a MAT 253 mass spectrometer (Thermo Fisher Scientific). The $\delta^{13}C$ and $\delta^{18}O$ values were calculated as deviations from laboratory standard referred to the PDB scale and reported in ‰ relative to V-PDB. The reproducibility was confirmed by replicate analyses of laboratory standards as being usually better than ±0.02‰ for $\delta^{13}C$ and $\delta^{18}O$ (1SD). In case of larger uncertainties of individual sample measurements, typical for impure materials, the higher value is presented.

U–Th geochronology

This study is based on U–Th age data determined for rather small samples (5.5 to 55.5 mg aliquots of the XRD and light stable isotope samples) in order to combine high structural resolution with the analytical precision of MC-ICP-MS. The U–Th isotope measurements

were performed on a VG Elemental AXIOM MC-ICP-MS at GEOMAR applying the multi-static MIC (multi-ion-counting)-ICP-MS approach after Fietzke et al. (2005). For isotope dilution measurements a combined $^{233/236}U/^{229}Th$-spike was used, with stock solutions calibrated for concentration using NIST-SRM3164 (U) and NIST-SRM3159 (Th) as combi-spike calibrated against CRM-145 uranium standard solution (also known as NBL-112A) for U-isotope composition, and against a secular equilibrium standard (HU-1, uranium ore solution) for determination of $^{230}Th/^{234}U$ activity ratio. Whole procedure blank values of this sample set were measured around 0.1 fg for ^{230}Th, around 7 pg for ^{232}Th and between 3 and 10 pg for U, which are in the typical range of this method and laboratory. Element separation procedure was based on Eichrom-UTEVA resin. Calculation of geochronological data and activity ratios is based on the decay constants given by Cheng et al. (2000).

From all original MASOX subsamples powder aliquots were attacked by 4 N acetic acid in order to provide weak leachates mainly dissolving the carbonate phase. Accepting that fractionation of U and Th may lead to a potential loss of ^{230}Th due to their difference in particle reactivity, these weak leachates result in minimum values in the direct $^{230}Th/^{234}U$ age determination. Where available, an additional powder aliquot of the original sample (marked by sample code suffix -2) was attacked by 2.25 N HNO_3 to provide a stronger leachate and potentially significant isochron spread. The 2.25 N HNO_3 attack was the only one applied to two aragonite-dominated HyBIS samples (s. Table S2).

Runs of aliquots of the HU-1 equilibrium standard solution to verify procedure reproducibility accompanied each set of element separation. A methodology dependent uncertainty of less than 0.5% on $^{230}Th/^{234}U$ activity ratios was reached. The geochronological uncertainties presented here are dominated by the analytical error of individual sample measurements and the uncertainty of correction factors. The applied data reduction includes a correction for isotopic composition of incorporated Th of detrital origin, according to average continental crust values (Wedepohl, 1995) as approximation for involved shelf sediments (s. notes under the Table S2 for details). For the majority of the sub-samples the uncertainty of this correction is negligible, but some are dominated

and even overcompensated to negative $^{230}Th/^{234}U$ activity ratios, due to low $^{230}Th/^{232}Th$ activity ratios and extreme high Th concentrations. An additional, more exact determination of potentially deviating isotope signatures of dissolved Th in the precipitation feeding cold seep fluid is hampered by the lack of adequate fluid sample material. An alternative, site-specific approach for isochron-based Th corrections, applicable for cold seep carbonates with elevated Th content is presented in a detailed small-scale case study by Bayon et al. (2009). The different scope and related sample selection strategy of our study is focused on direct age determination of single phases of predominately aragonitic composition as discussed in Liebetrau et al. 2010. However, Rosholt and Osmond isochron approaches presented here are based on the isoplot 3.75 software of the Berkeley Geochronology Center (CA, USA; Ludwig, 2008) and provide age estimates for two-point reference lines. The corresponding accuracy and reliability is limited by the fact that the measurements of the individual inherited detrital phase and adjacent pure sediment could not be finished during this initial measurement session. The $^{234}U/^{238}U$ ratios are presented in $\delta^{234}U$ notation (s. notes under Table S2 for details).

Geochronological implications

Characterized by generally low $^{230}Th/^{232}Th$ activity ratios, high Th concentration and low Ca-carbonate content, only few weak leachates provide the potential for single minimum age determination.

At $^{230}Th/^{232}Th$ activity ratios from 4.7 to 2.2 and $\delta^{13}C$ values from -41 to -32 ‰ (V-PDB) deduced single ages for MASOX samples are 6.6 ± 0.4 kys (SV21), 11.9 ± 2.6 kys (SV23-1), 3.4 ± 0.3 kys (SV28) and 5.0 ± 1.1 kys (SV29) BP. These data are supported by individual 2-point isochron reference lines of different leachates and parallel samples, covering at least similar age ranges (s. Table S2). The two latter samples are dominated by aragonite and represent the surface exposed today. Especially SV29, the most reliable aragonitic sample, reflects an age of authigenic carbonate precipitation similar to the findings on solidified material within the upper GC-section (SV21).

With the caveat that the heterogeneous carbonates result in considerable uncertainty, the deduced ages for the GC-samples increase systematically with depth suggesting a precipitation front following the prograding sediment deposition. The indicated age difference of approximately 5 kys between SV21 and SV23 and their depth difference of approximately 50 cm indicate a sedimentation rate around 0.1 mm/y, which is in accordance with outer shelf environments.

The shallowest and almost unconsolidated GC-sample with highest $\delta^{13}C$ values of -27 ‰ (V-PDB) at lowest leachate yields of only 6 to 13 % (SV20) and $^{230}Th/^{232}Th$ activity ratios around 1 seems to represent the least mature sample of this data set. This sample does not provide a reliable single age determination. However, a distinct isochron reference line suggests a precipitation phase around 0.55 ± 0.04 kys BP, the youngest found so far. The 3-dimensional (3D-Rosholt1) and 2-dimensional (Osmond) isochron reference lines (s. Table S2 for all required isotope ratios) provide important additional age indications, but due to the restriction on 2-point correlations the results are hampered by system-immanent underestimation of the uncertainties as their spread is dominated by the relatively precise individual isotope measurements of two subsamples and not by the potentially much larger distortion of the correlation coefficient from further subsamples.

However, independent support of the early onset of methane emanation stems from two aragonite dominated surface samples from the HyBIS site reflecting low $\delta^{13}C$ values around -37 ‰ (V-PDB) and U-Th ages of 8.2 ± 0.5 kys BP (SV-2) and 4.6 ± 0.5 kys BP (SV-3) at rather high $^{230}Th/^{232}Th$ activity ratios of 5.12±0.07 and 3.44±0.04, respectively, when compared to the MASOX values (s. Table S2). The U measurements for these two samples were performed on a quadrupole – inductively coupled plasma – mass spectrometer (Q-ICP-MS).

Table S2: U-Th isotope systematics and light stable isotope data of carbonate- enriched sediments at MASOX and HyBIS sites.

U-Th isotope systematics and light stable isotope data of carbonate enriched sediments at MASOX and HyBIS sites

Site (8)	$\delta^{234}U_{(o)}$ (5)	h)

Supplement 3: Fate of emitted methane in the water column

At the gas flares, significant amounts of methane were liberated into the water column, leading to bottom water CH_4 concentrations of up to 825 nM and a net flux of methane to the atmosphere. A fraction of CH_4 was consumed at rates of up to 3.06 nM d^{-1} (Fig. S3) in the lower part of the water column, but CH_4-concentrations in the well-mixed surface waters (~9 nM) were still generally exceeding the atmospheric equilibrium of ~3 nM. This excess indicates that the seeps off the coast of Svalbard are a net - though small - CH_4-source to the atmosphere.

Water column samples were collected from discrete depths at the MASOX and the HyBIS sites (Fig. 1) with a CTD/Rosette sampler equipped with 24 10-litre Teflon-lined Niskin bottles and a CTD device (Seabird SBE 9). Immediately upon recovery, we subsampled the Niskin bottles for on-board measurement of CH_4 concentrations and aerobic methane oxidation (MOx) rates. Methane concentrations were determined with a headspace method from ~ 600 ml aliquots, which were subsampled bubble-free into triple-layer Evarex Barrier Bags (Oxford Nutrition, U.K.). A high-purity nitrogen headspace (20 ml) was added, and samples were vigorously shaken and allowed to equilibrate for several hours before subsampling 2 ml headspace for CH_4 quantification with a gas chromatograph (GC, Agilent 7890A) equipped with a packed stainless steel column (6 ft., 2 mm i.d.; 80/100 mesh HayeSep Q) and a flame ionization detector. The GC was operated isocratically (60°C) with N_2 as carrier gas (33 ml min^{-1}). The analytical error of CH_4 concentrations is ±5 % (standard deviation) as determined from triplicate subsamples. Seawater methane concentrations and the degree of saturation with respect to the atmospheric equilibrium were calculated with consideration of sample/headspace volume, temperature, salinity, atmospheric pressure and atmospheric CH_4 mixing ratio (Wisenburg and Guinasso, 1979; Fisher et al., 2011). MOx rates were measured with a radio-tracer (^3H-CH_4) based assay (Reeburgh et al., 1991, Valentine et al., 2001). Subsamples were collected in quadruplicate in 20 ml crimp top serum glass vials and sealed bubble-free with bromo-butyl stoppers (Helvoet Pharma, Belgium). Each subsample was amended with ^3H-labelled CH_4 (10 µl

494 CH_4/N_2 mixture: ~25 kBq, <50 pmol CH_4, American Radiolabeled Chemicals, USA) within a
495 few h after subsampling and incubated for 72 h at *in situ* T (~4°C) in the dark. Total activity
496 (^3H-CH_4 + ^3H-H_2O) was subsequently determined from a 2 ml sample aliquot by wet
497 scintillation. The remaining sample was purged for 30 min with a constant stream of air (~
498 50 ml min^{-1}) to remove unreacted CH_4 before measuring the activity of ^3H-H_2O from a 2 ml
499 aliquot. We calculated MOx rates from the fractional turnover of labeled CH_4 and water column
500 CH4 concentrations assuming first order kinetics. MOx rates were corrected for
501 (insubstantial) tracer turnover in killed controls (amended with 100 µl, saturated HgCl).

502 Methane concentrations were highest in bottom waters (Fig. S3 a) and decreased towards
503 the sea surface. MOx rates showed similar trends (Fig. S3 b). However, MOx rates were
504 substantially lower at the HyBIS site despite a ~10-fold higher bottom water CH_4
505 concentrations. The decrease in CH_4 concentrations from seafloor to surface samples thus
506 appears to be controlled by MOx as well as other factors, probably dilution and horizontal
507 mixing by bottom currents. Nevertheless, CH_4 concentrations in the well-mixed surface
508 waters (sampled at 4-5 m water depth, ~9nM) were supersaturated with respect to the
509 atmospheric equilibrium (3nM; calculated using Bunsen solubility coefficients from
510 Wiesenburg and Guinasso, 1979 and local atmospheric methane concentrations from
511 Fisher et al., 2011) indicating a net CH_4 efflux from the water column above the Svalbard
512 seeps to the atmosphere at least during the time of observation (Wanninkhof et al., 2009).
513 However, efflux from ~300% methane saturation of surface waters was not found to
514 produce pronounced local atmospheric methane anomalies in a study from the Black Sea
515 (Schmale et al., 2005). Thus, the influence on the local atmospheric methane budget of the
516 Svalbard seeps is probably minor.

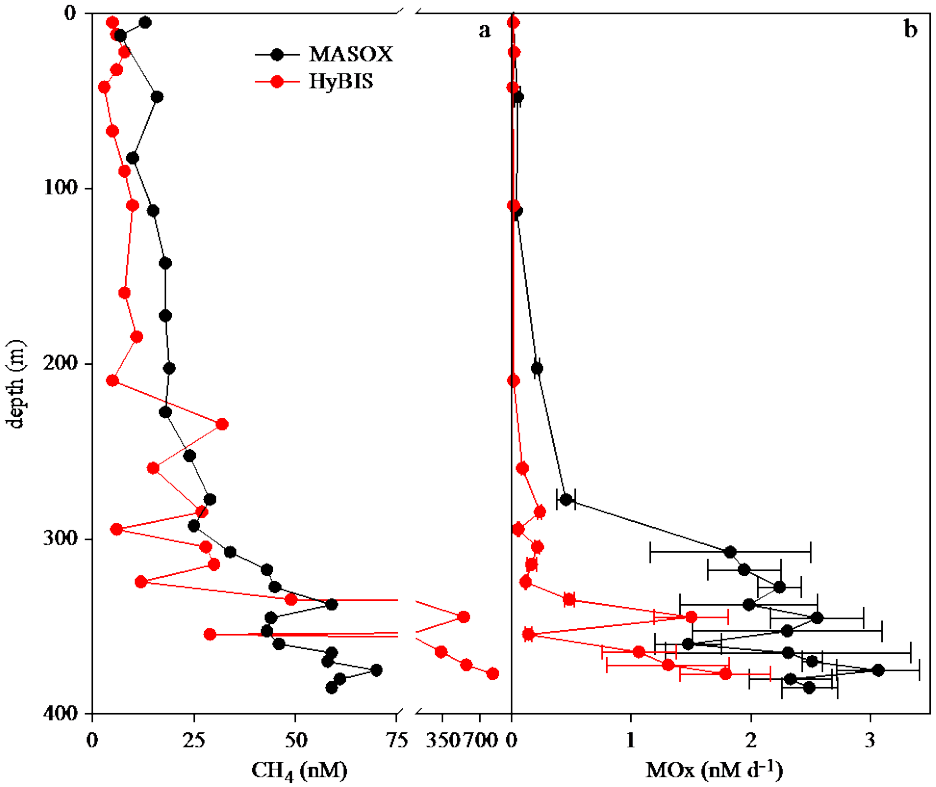

517

518 **Fig. S3**. Vertical profiles of methane concentrations (a) and rates of aerobic methane
519 oxidation (b) in the water column at two active seepage sites off the coast of Svalbard.
520 Errors are represented as standard deviation. Methane concentrations and rates of aerobic
521 methane oxidation were variable but generally highest in bottom waters.

522

523 ## Supplement 4: Geochemical analyses of surface sediments

524 Sediments were collected at the HyBIS and MASOX sites either with push cores (i.d. 60 and
525 26 mm) operated by the submersible JAGO or with a gravity corer (i.d. 120 mm). Push
526 cores were taken in areas of visible gas releases and the presence of chemosynthetic
527 communities (sulfur bacteria mats, frenulate tubeworms, see Suppl. Fig. S4). The gravity
528 core at the MASOX site was taken at a location at which gas flares were observed in the
529 water column on EK60 profiles just prior to coring, and where the presence of extensive

sulfur bacteria mats was confirmed by JAGO dives. From the 60 and 120 mm cores, a sediment sample of 2 cm^3 was taken with a cut-off plastic syringe to determine the methane concentration. The sample was then transferred into a 10 mL glass vial filled with 5 mL sodium hydroxide (2.5% w/w). The vial was closed immediately with a butyl rubber stopper, sealed with an aluminum crimp, and shaken thoroughly to equilibrate the pore water methane between the aqueous and the gaseous phases. After equilibration, the methane concentration of the sample was analyzed with a gas chromatograph equipped with a flame ionization detector. Sediment pore water was squeezed from sediment sections of the 60 and 120 mm cores using a pressure filtration system at pressures up to 5 bar and filtered through 0.45 µm cellulose acetate membrane filters. Pore water samples were then immediately analyzed onboard to determine total alkalinity (Ivanenkov and Lyakhinand 1978) and sulfide concentrations (Cline 1969). Rates of anaerobic oxidation of methane (AOM) were determined in the 26 mm cores using the whole-core injection method (Jørgensen, 1978). Radioactive methane tracer (aliquots of 5 kBq $^{14}CH_4$ dissolved in 15 µl water) were injected into the cores in 1-cm-intervals. The cores were incubated at in situ temperature for 24 h in the dark. After incubation, reactions were terminated by fixing 1 cm-sections in 2.5% sodium hydroxide. In control samples, activity was terminated before tracer addition. Methane oxidation rates were determined by gas chromatography, $^{14}CH_4$ combustion and $^{14}CO_2$ acidification as described in detail by Treude et al. (2005).

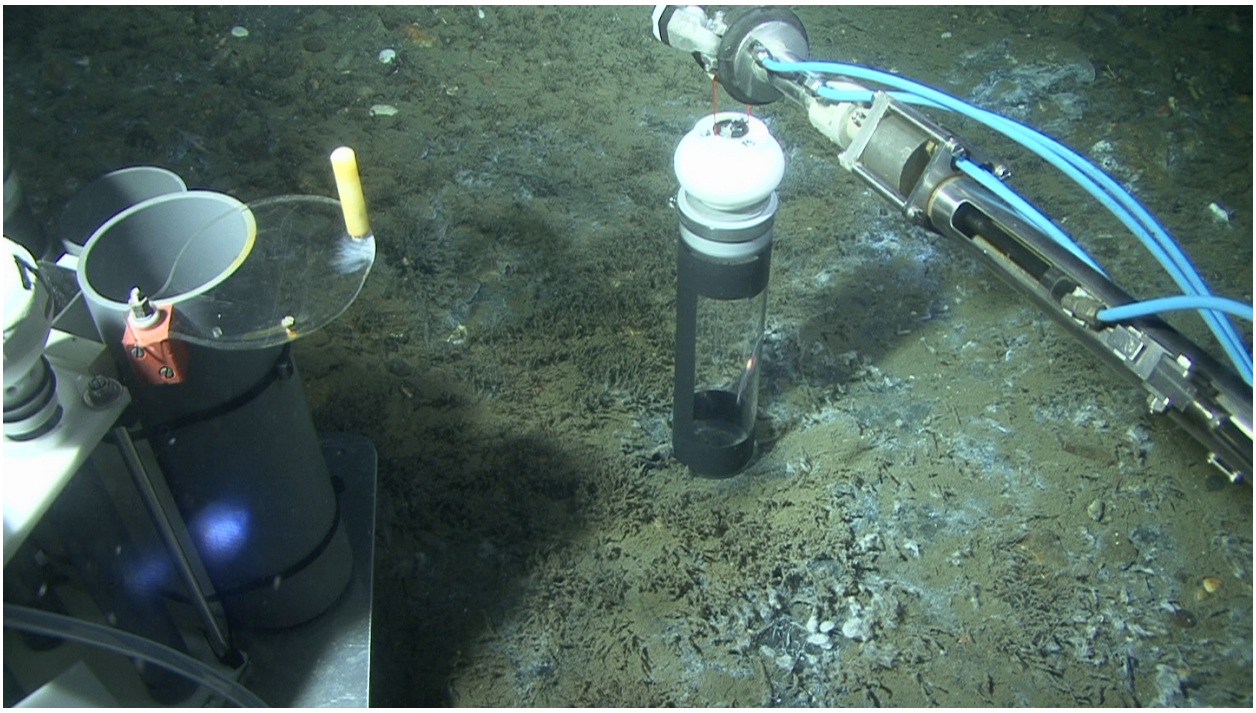

Fig. S4. Deployment of a sediment pushcore by the submersible Jago in a methane seep field at the HyBIS site. The sediment is covered by sulfur bacteria mats (white) and frenulate tubeworms (grass-like structures), which are typically found at methane seep locations featuring high activity of anaerobic oxidation of methane in the surface sediment (e.g. Treude et al. 2003, Niemann et al. 2006).

References used in the supplements

Bayon, G., Henderson, G.M., Bohn, M., 2009. U–Th stratigraphy of a cold seep carbonate crust. *Chemical Geology*, 260, 47–56.

Cline, J.D., *Spectrophometric determination of hydrogen sulfide in natural waters.* Limnol. Oceanogr., 1969. **14**: p. 454-458.

Cheng, H., Edwards, R.L., Hoff, J., Gallup, C.D., Richards, D.A., Asmerom, Y., 2000. The half-lives of uranium-234 and thorium-230. *Chemical Geology*, 169, 17–33.

563 Fietzke, J., Liebetrau, V., Eisenhauer, A., Dullo, W.-C.h., 2005. Determination of Uranium
564 isotope ratios by multi-static MIC-ICP-MS: method and implementation for precise U-
565 and Th-series isotope measurements. *Journal of Anal. Atom. Spectrom*. 20, 395–401.

566 Fisher, R. E., S. Sriskantharajah, D. Lowry, M. Lanoisellé, C.M.R. Fowler, R.H. James, O.
567 Hermansen, C. Lund Myhre, A. Stohl, J. Greinert, P.B.R. Nisbet-Jones, J. Mienert, and
568 E.G. Nisbet. 2011. Arctic methane sources: Isotopic evidence for atmospheric inputs.
569 Geophysical Research Letters 38: L21803-L2180.

570 Ivanenkov, V.N. and V.N. Lyakhin, 1978. *Determination of total alkalinity in seawater*, in
571 *Methods of hydrochemical investigations in the ocean (in Russian)*, O.K. Bordovsky
572 and V.N. Ivanenkov, Editors. Nauka Publ. House: Moscow. 110-114.

573 Jørgensen, B. B. 1978. A comparison of methods for the quantification of bacterial sulphate
574 reduction in coastal marine sediments: I. Measurements with radiotracer
575 techniques. Geomicrobiol. J. 1(1): 11-27.

576 Liebetrau, V., Eisenhauer, A., Linke, P. 2010. Cold seep carbonates and associated coldwater
577 corals at the Hikurangi Margin, New Zealand: New insights into fluid pathways,
578 growth structures and geochronology. Marine Geology, 272, 307 – 318.
579 doi:10.1016/j.margeo.2010.01.003.

580 Ludwig K.R., 2008. Isoplot 3.7: A Geochronological Toolkit for Microsoft Excel. Berkeley
581 Geochronology Center Spec. Publ., 4.

582 Reeburgh, W. S., B.B. Ward, S.C. Whalen, K.A. Sandbeck, K.A. Kilpatrick, and L.J. Kerkhof.
583 1991. Black-Sea Methane Geochemistry. Deep-Sea Research Part a-Oceanographic
584 Research Papers 38: 1189-1210.

585 Schmale, O., J. Greinert, and G. Rehder, 2005. Methane emission from high-intensity marine
586 gas seeps in the Black Sea into the atmosphere, Geophysical Research Letters, 32 (7),
587 L07609.

588 Treude, T., M. Krüger, A. Boetius and B. B. Jørgensen, 2005. Environmental control on
589 anaerobic oxidation of methane in the gassy sediments of Eckernförde Bay (German
590 Baltic). Limnol. Oceanogr. 50: 1771-1786.

591 Treude, T., A. Boetius, K. Knittel, K. Wallmann and B. B. Jørgensen, 2003. Anaerobic
592 oxidation of methane above gas hydrates at Hydrate Ridge, NE Pacific Ocean. Mar.
593 Ecol. Prog. Ser. 264: 1-14.

594 Niemann, H., T. Lösekann, D. De Beer, M. Elvert, T. Nadalig, K. Knittel, A. Aman, E. J. Sauter,
595 M. Schlüter, M. Klages, J.-P. Foucher and A. Boetius, 2006. Novel microbial
596 communities of the Haakon Mosby mud volcano and their role as a methane sink.
597 Nature 443: 854-858.

598 Valentine, D. L., D.C. Blanton, W.S. Reeburgh, and M. Kastner. 2001. Water column methane
599 oxidation adjacent to an area of active hydrate dissociation, Eel River Basin.
600 Geochim. Cosmochim. Acta 65: 2633-2640.

601 Villinger, H. & Davis, E. 1987. A new reduction algorithm for marine heat flow
602 measurements. J. Geophys. Res 92, 846–856.

603 Wanninkhof, R., W.E. Asher, D.T. Ho, C. Sweeney, and W.R. McGillis. 2009. Advances in
604 Quantifying Air-Sea Gas Exchange and Environmental Forcing. Annual Review of
605 Marine Science 1: 213.

606 Wedepohl, K.H., 1995. The composition of the continental crust. *Geochimica et Cosmochimica*
607 *Acta,* 59 (7), 1217–1232.

608 Wiesenburg, D.A. and Guinasso, N.L. 1979. Equilibrium solubilities of methane, carbon
609 monoxide, and hydrogen in water and sea water. J. Chem. Eng. Data. 24 (4), 356-360.

610 Woodside, W. & Messmer, J.H. 1961. Thermal conductivity of porous media. I.
611 Unconsolidated sands. J. Appl. Phys. 32, 1688-1699.